Novel Design of Permanent Magnet-Assisted Synchronous Reluctance Motor Using Metal Additive Manufacturing Technology

Md Jabed Hossain, Paxton Schroeder
and Roy A McCann
Department of Electrical Engineering
and Computer Science (EECS)
University of Arkansas
Fayetteville, USA

***Abstract*—This paper presents an advanced design and investigation of a Permanent Magnet Assisted Synchronous Reluctance Motor (PM-Assisted-SynRM). This unique design incorporates a two-level permanent magnet flux barrier to secure the permanent magnet, accompanied by an additional third-level flux barrier, aiming to achieve a sinusoidal air-gap flux density. The main innovation involves introducing a higher number of stator slots to enhance output power density. These stator slots are designed to house rectangular copper windings, thereby increasing the slot fill factor. The consideration of a single turn in each slot is explored to minimize dv/dt interference and enable the utilization of higher frequency power electronics drives. The challenges in manufacturing complex geometry stator and rotor laminations are addressed through the application of metal additive manufacturing technology. The efficacy of the proposed model is evaluated by validating its characteristics, including output torque, torque ripple, radial air-gap flux density, cogging torque, static torque, and back-EMFs, through finite element analysis (FEA).**

Keywords—Finite element analysis (FEA), analytical design, PM-Assisted-SynRM, flux barrier (FB), torque ripple, back EMFs.

I. Introduction

The PM-Assisted-SynRM has attracted considerable attention for combining the advantages of Permanent Magnet Synchronous Motors with Synchronous Reluctance Motors. PM-Assisted-SynRM are widely utilized in industrial drive, electric vehicles, and aerospace, because of their characteristics, including high power density, efficiency, a wide speed range, minimal reliance on permanent magnets (PMs), compact size, and lightweight design [1, 2]. The common rotor configuration for PM-Assisted-SynRM utilizes a multi-layer flux barrier, and a complex rotor structure, contributing to torque ripple that could cause noticeable noise, vibration, and a short lifespan [3].

Numerous studies in the literature address the reduction of torque ripple and the limiting of vibration. A model encompassing electromagnetic, structural, and acoustic aspect has been created to assess the noise and vibration characteristics of electrical machines [4]. The application of the PM shifting technique focuses on reducing torque ripples, and combining this technique with an appropriate flux barrier open angle is designed to improve torque capability [5]. Research findings suggest that adjusting the position of the reluctance axis within an irregular rotor core leads to the magnet-axis-shift effect [6]. Bianchi et al [7] presented various configurations of flux barriers based on their respective polarities. Sanada et al. [8] utilized an asymmetrical arrangement of flux barriers intentionally misaligning their outer edges with the teeth, aiming to reduce torque ripple. It has been shown that the utilization of an arc-shaped flux barrier is advantageous for PM-Assisted-SynRM in achieving higher torque and power density [9, 10]. Jabed et al. demonstrated the integration of higher number of stator slots in both IPM motors [11] and SPM motors [12].

There is limited research in the current literature that addresses both the reduction of torque ripple and the simultaneous increase in output torque density. This study aims to alleviate the torque ripple and enhance output power density by introducing a novel design for PM-Assisted-SynRM. The main goals of this project can be outlined as follows:

- Introducing a higher number of stator slots to improve the output power density.
- Employing rectangular stator slots to enhance the slot fill factor. Each stator slot features a single-turn coil, reducing parasitic capacitance and facilitating high-frequency power electronics drive.
- Proposing a novel rotor design to achieve a sinusoidal air-gap flux density and minimize cogging torque.
- Utilizing metal additive technology for the manufacturing of the complex geometry of rotor and stator lamination. Detailed manufacturing information is presented in the concluding section.

II. Design of PM-Assisted-SynRM

A. Novel PM-Assisted-SynRMs

Fig. 1 depicts a single pole of a PM-Assisted-SynRM, featuring a distributed winding with a total of 90 slots and 6 poles. The rotor lamination is composed of three layers of flux barriers in each pole, and the rotor magnets are positioned between two flux barriers using magnets of two different dimensions, arranged in an asymmetrical manner. The stator and rotor core laminations use the steel sheet M19_26G. The details of the proposed topology specifications can be found in Table I.

B. Design Basics of PM-Assisted-SynRMs

The expression of the torque equation of PM-Assisted-SynRM in the d-q reference frame is presented as follows:

$$T_e = \frac{3}{2}\frac{p}{2}\left(L_d - L_q\right)I_d I_q + \frac{3}{2}\frac{p}{2}\lambda_m I_q \qquad (1)$$

This work was supported in part by the U.S. National Science Foundation under award no. 2230857 as part of the I-Corps program.

2024 IEEE Green Technologies Conference (GreenTech) | 979-8-3503-0858-7/24/$31.00 ©2024 IEEE | DOI: 10.1109/GREENTECH58819.2024.10520449

TABLE I
IMPORTANT DESIGN PARAMETERS OF PROPOSED MODELS

Parameters	Unit	Value
Outer diameter of stator	mm	120
Inner diameter of stator	mm	69.5
Outer diameter of rotor	mm	68.4
Airgap	mm	0.55
Rated speed	rmp	1890
Rated torque	Nm	7.96
Rated power	kW	1.65
Number of turns per coil		1
Stack length	mm	40.029
No. of poles		6
No. of slots		90
No. of phases		3
Magnet grade		NdFeB
Rotor & Stator core materials		M19_26G

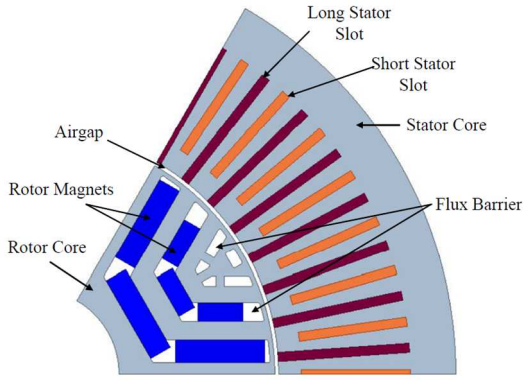

Fig. 1. One-sixth of proposed PM-Assisted-SynRM.

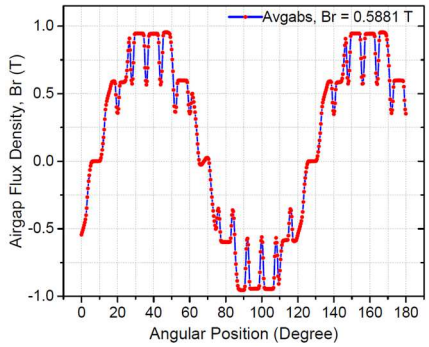

Fig. 2. Air-gap flux density resulting solely from magnetic loading.

here, the subscripts d and q denote the direct and quadrature axis, respectively. L_d and L_q stand for the inductances, I_d and I_q represent the currents, λ_m is the PM flux linkage, p signifies the number of poles.

The expression for torque ripple of a PM-Assisted-SynRM is given by,

$$T_{ripple} = \frac{T_{p-p}}{T_{ave}} \tag{2}$$

where, T_{p-p} signifies peak to the peak value of torque, while T_{ave} indicates mean torque.

Electrical loading was computed using the following equation:

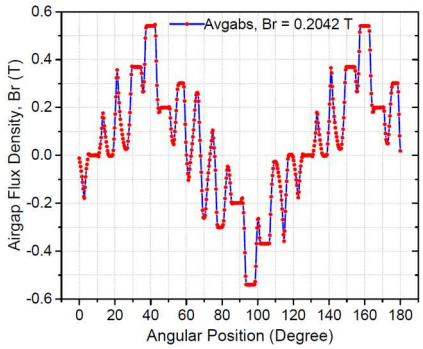

Fig. 3. Distribution of air-gap flux density due to electrical loading only.

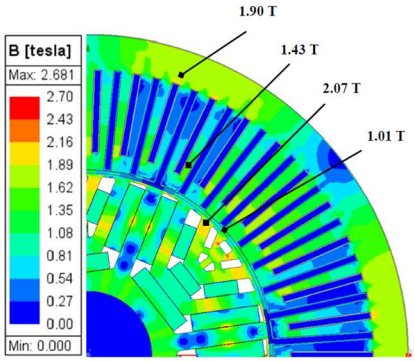

Fig. 4. Distribution of flux density at different places. .

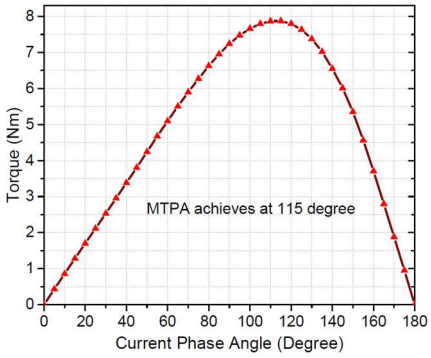

Fig. 5. Static-torque and MTPA angle calculation.

$$ac = \frac{3 \times 2 \times N_{tc} \times N_{cpph} \times I_c}{\pi D} \tag{3}$$

I_c symbolizes the coil current, N_{tc} stands for the number of turns in each coil, D represents the stator bore diameter, and N_{cpph} denotes the number of coils per phase.

The formula for phase back EMFs can be stated as:

$$E_{ph} = 4.44 \times f_s \times N_{etpph} \times k_w \times \varphi_p \tag{4}$$

In this equation, f_s stands for the rated supply frequency, N_{etpph} indicates the number of effective turns per phase, k_w represents the winding factor, φ_p corresponds to flux per pole.

Eddy current and hysteresis losses are computed for two distinct regions, namely, stator tooth and stator yoke. The calculation of eddy current loss is performed using the following equation.

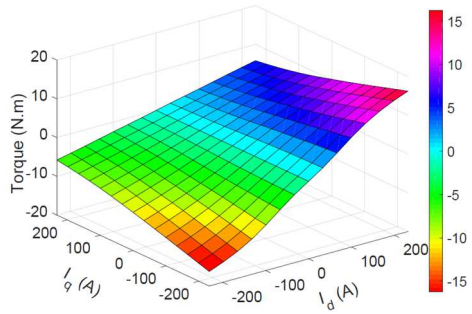

Fig. 6. Torque calculation by varying Id and Iq currents .

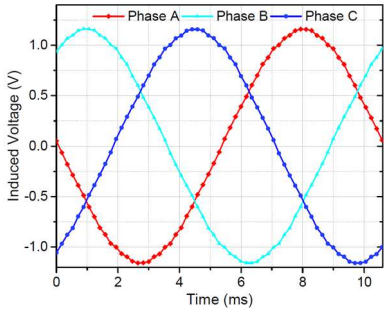

Fig. 7. Waveforms of no-load three-phase back EMFs.

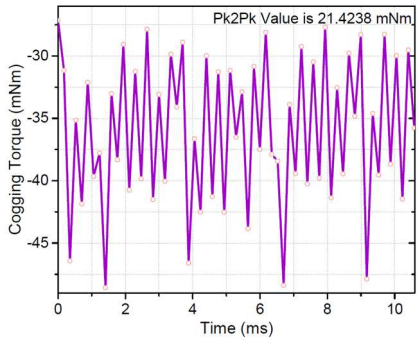

Fig. 8. Cogging torque of the proposed PM-Assisted-SynRM.

$$P_{eddy\_st} = K_e \times f_s^2 \times B_{sa}^2 \times V_{sa} \quad (5)$$

where, K_e represents the eddy current loss-coefficient of steel, B_{sa} denotes the maximum flux density of the corresponding area, and V_{sa} is the volume of the corresponding area. Likewise, the hysteresis loss was determined using the following equation:

$$P_{hyst\_st} = K_h \times f_s^{\alpha} \times B_{st}^{\beta} \times V_{st} \quad (6)$$

where, α, β, and K_h symbolize the hysteresis loss-coefficient of steel. B_{sa} represents the maximum flux density of the corresponding area, while V_{sa} indicates the volume of that specific area.

III. Analysis of Result

A. Computing Radial Air-gap Flux Density

1) Due to Only Magnet Flux: A magnetostatics finite element analysis (FEA) was conducted, where the stator current was intentionally set to zero. The main focus was on assessing the radial flux density produced exclusively by the rotor magnet. The air-gap flux densities in the proposed model is illustrated in Fig. 2. The observed flux density in the air-gap of the proposed PM-Assisted-SynRM exhibits a sinusoidal pattern, indicating lower harmonic content. This characteristic contributes to the reduction of the cogging torque component. The average air-gap flux density is computed as 0.588 T, slightly exceeding the analytical value of 0.56 T.

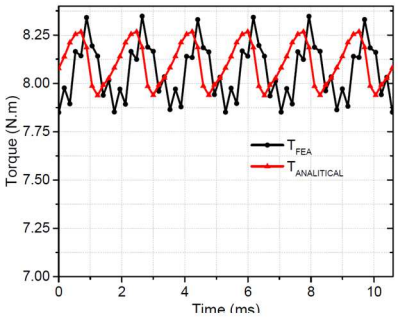

Fig. 9. Comparison of torque characteristics between FEA and an analytical calculation of the proposed PM-Assisted-SynR.

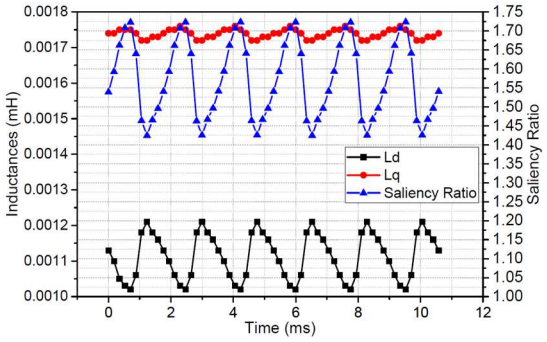

Fig. 10. Inductances and saliency calculation.

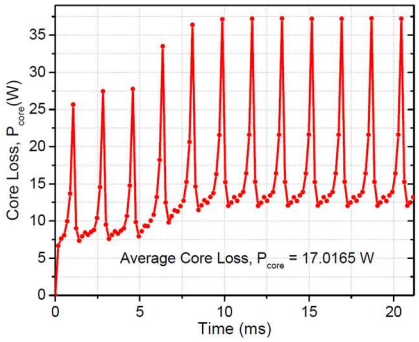

Fig. 11. Hysteresis loss calculation .

2) Effect of Armature Field Only: Another FEA was carried out to evaluate the air-gap flux density induced radially solely by the stator current, utilizing an electrical loading of 45 kA/m. Notably, the analysis deliberately excluded the magnets from the rotor. As shown in Fig. 3, the calculated mean radial flux density at the air-gap, resulting exclusively from electrical loading, was found to be 0.204 T. This value closely corresponds to the intended target.

3) Flux Density at Different Areas: A magnetostatics simulation was performed under full load conditions to visualize the flux density at different regions of the motor. As presented in Fig. 4, the flux density at various areas is

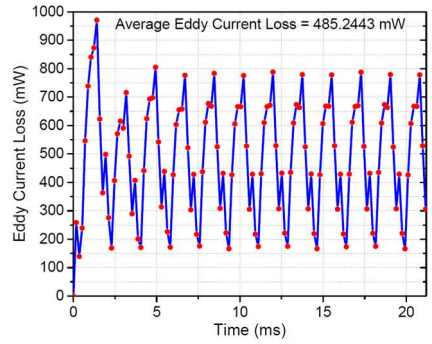

Fig. 12. Eddy current loss calculation of proposed model.

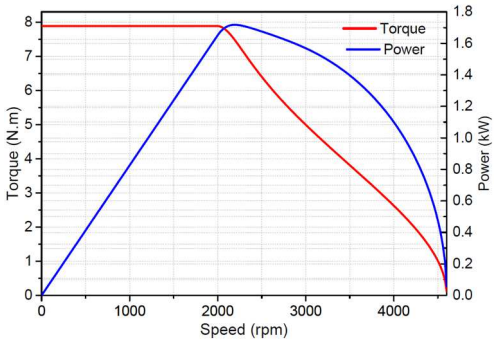

Fig. 13. Torque-speed and power-speed curve of the proposed model. .

displayed. The maximum flux density near the rotor rib attains 2 T, followed by the stator back iron exhibiting a flux.density of 1.90 T.

B. Static Torque and MTPA Calculation

The angle and strength of the stator's magnetic field are affected by the phase angle of the stator current. In this project, the Maximum Torque Per Ampere (MTPA) controlling method is utilized. A parametric sweep simulation, ranging from 0 degrees to 180 degrees of the phase current angle with 5-degree increments, was conducted to identify the MTPA angle. The phase current angle at which the maximum torque is attained is determined. As illustrated in Fig. 5, the maximum torque is achieved at 115 degrees, measuring 7.98 N.m. This torque value closely aligns with the desired analytical value. Another parametric sweep simulation verifies the computation of the MTPA angle. In this simulation, torque is calculated by varying I_d and I_q. It is shown in Fig. 6 that at 115 degrees (an advance angle of 25), the torque achieved is 7.98 N.m, consistent with the previous analysis.

C. No-Load Simulation

1) No-Load Back EMFs Calculation: The increased air-gap flux density produced by the permanent magnet leads to a rise in the magnitude of back-EMF in each phase. Fig.7 illustrates the no-load back-EMF characteristics of the proposed model. The root mean square (RMS) value for the back-EMF in the proposed topology is 0.8039 V, slightly surpassing the analytical topology's back-EMF RMS of 0.8499 V calculated by (5).

2) Cogging Torque Calculation: A further no-load transient simulation was performed to examine the cogging torque characteristics of the novel design. As depicted in

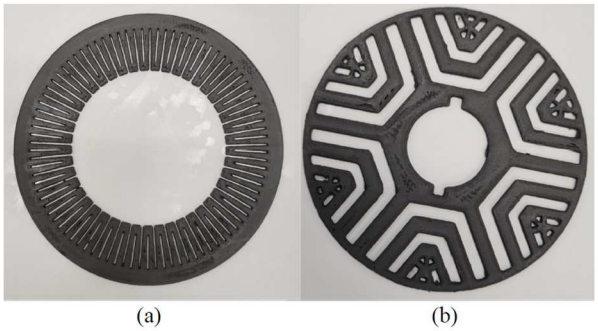

Fig. 14. Printed output (a) Stator lamination (b) Rotor lamination. .

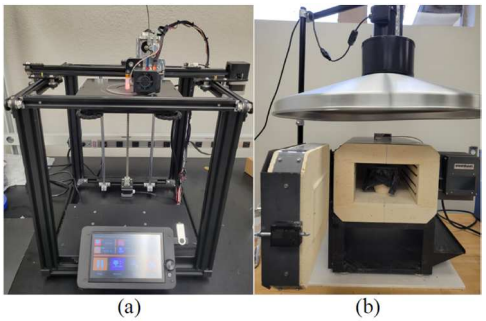

Fig. 15. Lab setup (a) 3D metal printer (b) Kiln

Fig.8, the cogging torque is shown at a speed of 1890 rpm. The calculated cogging torque falls within the desired range.

D. Steady State Simulation

1) Output Torque Characteristics: The characteristics of electromagnetic torque are obtained through a steady-state simulation at 149 A and 1890 rpm. The proposed PM-Assisted-SynRM, as per the FEA value, demonstrates an average torque close to the desired value but with a slightly larger torque ripple. Fig. 9 provides a comparison of torque characteristics between FEA and Analytical values, where Analytical values are calculated by (1).

2) Saliency Ratio Determination: In Fig. 10, a comparison is shown between the d-axis and q-axis inductances, as well as the saliency ratio of the PM-Assisted-SynRM obtained from steady-state simulation. As expected, the q-axis inductance of the PM-Assisted-SynRM consistently exceeds the d-axis inductance, as anticipated. The calculated average saliency ratio is 1.57.

3) Core Loss Calculation: Eddy current loss and hysteresis loss are determined by (5) and (6), respectively. The FEA values are subsequently compared with analytical values in Table II. The average hysteresis loss and eddy current loss, as computed using FEA, amount to 17.01 W and 0.485 W, respectively, as depicted in Fig. 11 and Fig. 12.

4) Torque-Speed/Power-Speed Curve: The torque-speed and power-speed curves are derived using a novel approach. As shown in Fig. 13, the proposed PM-Assisted-SynRM demonstrates constant torque in the constant-torque region and is capable of attaining high speeds in the field weakening control region. The maximum torque of the PM-Assisted-SynRM remains relatively constant up to rated speed of 1980

TABLE II
COMPARISON OF ANALYTICAL VALUES WITH FEA VALUES

Parameters	Unit	Analytical Value	FEA value
Output Torque	N.m	8.0661	8.1079
Torque Ripple	%	6.18	4.07
Cogging Torque	mN.m(Pk2Pk)	10	38.5
Eddy Current Loss	W	3.2	0.485
Hysteresis Loss	W	13.60	17.01
Efficiency	%	92.38	91.98

rpm. Nevertheless, the power of the PMA-SynRM starts to decline after reaching 1980 rpm.

IV. PROTOTYPING

In this project, metal additive technology was utilized to produce the rotor, stator, and stator winding, addressing the challenge of creating complex geometries. The rotor and stator lamination are crafted from high-carbon iron, while the stator winding is made from copper material. Metal additive manufacturing involves three stages: i. printing, ii. debinding, iii. sintering. Fig. 14(a) and 14(b) depict the metal-printed stator and rotor lamination. Debinding is the procedure of eliminating additives from the molded component, ensuring the complete removal of primary binding materials before the sintering stage. Sintering is the process in which atoms within materials migrate across particle boundaries and fuse together into a unified piece. Fig. 15 illustrates the laboratory arrangement for prototyping the motor, with (a) displaying the 3D printer machine and (b) depicting the kiln.

A. Rotor & Stator Lamination Manufacturing

1) Debinding of High Carbon Iron: Steel blend refractory is used in the crucible for the debinding process of high carbon iron materials. It is essential to set the furnace temperature to rise at a rate of 93.33°C (200°F) per hour until it reaches 204°C (400°F). This temperature must be maintained for a duration of 2 hours. Additionally, another temperature ramp needs to be configured, where over a period of 2 hours, the temperature should gradually increase to 427°C (800°F), and subsequently, it should be held at 427°C (800°F) for an additional 2 hours.

2) Sintering of High Carbon Iron: Steel Blend serves as a refractory material within the crucible during the sintering process of high carbon iron materials. Additionally, Sintering Carbon is positioned on top of the crucible. The furnace temperature was set to increase at a rate of 333°C (600°F) per hour until it reached the sintering temperature of 1300°C (2372°F). The sintering temperature was then sustained for a duration of 4 hours.

B. Stator Winding Manufacturing

1) Debinding of Copper: AI_2O_3 refractory is employed within the crucible for the debinding process of copper materials. It is necessary to program the furnace temperature to increase at a rate of 55.6°C (100°F) per hour until it reaches 482°C (900°F). This temperature must be sustained for a duration of 4 hours.

2) Sintering of Copper: Magnesium Silicate acts as a refractory material inside the crucible for the sintering process of copper materials. Moreover, Sintering Carbon is placed on top of the crucible. The furnace temperature was programmed to rise at a rate of 111.1°C (200°F) per hour until reaching the sintering temperature of 1052°C (1925°F). Maintained the sintering temperature for a period of 5 hours.

V. CONCLUSION

This paper introduces a new configuration for PM-Assisted-SynRM aimed at enhancing output torque and achieving improved torque characteristics. The theoretical concept was applied to the proposed topology, and the validation of analytical results was confirmed through FEA simulations and other design variations. Subsequently, rotor and stator lamination are produced using metal additive manufacturing technology, and the manufacturing steps are outlined in this paper. The analyses indicate that the proposed model exhibits excellent electromechanical performance, making it as an ideal candidate for variable speed drive applications.

REFERENCES

[1] H. Guo et al., "Design of an aviation dual-three-phase high-power high-speed permanent magnet assisted synchronous reluctance starter-generator with antishort-circuit ability," IEEE Transactions on Power Electronics, vol. 37, no. 10, pp. 12619-12635, 2022.

[2] X. Liu, Y. Li, Z. Liu, T. Ling, and Z. Luo, "Analysis and design of a high power density permanent magnet-assisted synchronous reluctance machine with low-cost ferrite magnets for EVs/HEVs," COMPEL-The international journal for computation and mathematics in electrical and electronic engineering, vol. 35, no. 6, pp. 1949-1964, 2016.

[3] Y. Lu et al., "Comparative study on vibration behaviors of permanent magnet assisted synchronous reluctance machines with different rotor topologies," IEEE Transactions on Industry Applications, vol. 57, no. 2, pp. 1420-1428, 2021.

[4] J. Le Besnerais, "Vibroacoustic analysis of radial and tangential air-gap magnetic forces in permanent magnet synchronous machines," IEEE Transactions on Magnetics, vol. 51, no. 6, pp. 1-9, 2015.

[5] G. Liu, G. Xu, W. Zhao, X. Du, and Q. Chen, "Improvement of torque capability of permanent-magnet motor by using hybrid rotor configuration," IEEE Transactions on Energy Conversion, vol. 32, no. 3, pp. 953-962, 2017.

[6] H. Yang, W. Wang, H. Lin, Z. Zhu, S. Lyu, and S. Niu, "A novel hybrid-pole interior PM machine with magnet-axis-shifting effect," in 2019 IEEE International Electric Machines & Drives Conference (IEMDC), 2019: IEEE, pp. 273-279.

[7] N. Bianchi, S. Bolognani, D. Bon, and M. Dai Pre, "Rotor flux-barrier design for torque ripple reduction in synchronous reluctance and PM-assisted synchronous reluctance motors," IEEE Transactions on Industry Applications, vol. 45, no. 3, pp. 921-928, 2009.

[8] M. Sanada, K. Hiramoto, S. Morimoto, and Y. Takeda, "Torque ripple improvement for synchronous reluctance motor using an asymmetric flux barrier arrangement," IEEE Transactions on Industry Applications, vol. 40, no. 4, pp. 1076-1082, 2004.

[9] T. A. Huynh and M.-F. Hsieh, "Irreversible demagnetization analysis for multilayer magnets of permanent magnet-assisted synchronous reluctance machines considering current phase angle," IEEE Transactions on Magnetics, vol. 55, no. 7, pp. 1-9, 2019.

[10] R.-R. Moghaddam and F. Gyllensten, "Novel high-performance SynRM design method: An easy approach for a complicated rotor topology," IEEE Transactions on Industrial Electronics, vol. 61, no. 9, pp. 5058-5065, 2013.

[11] M. J. Hossain, K. Mackey, and R. A. McCann, "Enhancing Performance of Interior Permanent Magnet Motors Using Novel Stator Slot Designs," in 2023 North American Power Symposium (NAPS), 15-17 Oct. 2023 2023, pp. 1-6, doi: 10.1109/NAPS58826.2023.10318775.

[12] M. J. Hossain, F. M. Felizco, M. T. Sandjong, and R. A. McCann, "A Novel Higher Stator Slots Surface-Mounted Permanent Magnet Motor for Variable Speed Drives," in 2023 IEEE Industry Applications Society Annual Meeting (IAS), 29 Oct.-2 Nov. 2023 2023, pp. 1-5, doi: 10.1109/IAS54024.2023.10406350.